Supplementary Information for: Bayesian blacksmithing: Discovering thermomechanical properties and deformation mechanisms in high-entropy refractory alloys

Jacob Startt[1], Megan MCcCarthy[2], Mitch A. Wood[2], Sean Donegan[3], and Rémi Dingreville[*1,*]

[1]Center for Integrated Nanotechnologies, Nanostructure Physics Department, Sandia National Laboratories, Albuquerque, NM, 87185, USA
[2]Center for Computing Research, Computational Multiscale Department, Sandia National Laboratories, Albuquerque, NM, 87185, USA
[3]Air Force Research Labs, OH, USA
[*]rdingre@sandia.gov

ABSTRACT

This supplementary information contains details on: (i) Parameterization of atomistic simulations (Note 1), (ii) insights on configurational entropy (Note 2), (iii) insight on compositional effects (Note 3), (iv) validation of molecular dynamics models through DFT (Note 4).

Contents

[*]rdingre@sandia.gov

Note 1: Parameterization of molecular dynamics simulations

Bulk modulus

The performance of the MTP and SNAP potentials in modeling elasticity properties was benchmarked against DFT. The elastic constant matrix, $\mathbb{C}_{ijkl}$, was calculated for a set of alloy compositions, selected according to the grid formula $A_x(BCD)_{1-x}$, where x was incrementally increased from 12.5 at.% to 50 at.%. MD and DFT calculations determined the elastic constant matrix via the relationship between stress and strain, $\sigma_{ij} = \mathbb{C}_{ijkl} : \varepsilon_{kl}$. The simulations cells used in the MD calculations were identical in size, shape, and number atoms to those used in the optimization calculations. DFT $\mathbb{C}_{ijkl}$ matrices were calculated using randomly ordered $4 \times 4 \times 4$ supercells containing 128 atoms and DFT simulation parameters similar to what used in the DOS calculations. To account for finite ordering effects, each composition was modeled four times, each time using a differently ordered DFT supercell. To compare potential performance, the Voigt-Reuss-Hill elastic moduli averages were calculated from the $\mathbb{C}_{ijkl}$ matrix and plotted in Supplementary Figure 1. Moduli calculated via DFT represent the average modulus of the four distinct supercells. Each MD potential exhibited different characteristics in its ability to replicate the DFT values, allowing for several observations to be made. First, while each potential was able to capture the approximate trends of the DFT moduli (outside of a few exceptions which will be discussed shortly), the MTP potential consistently under-predicted the magnitude of the DFT moduli by ~10-15 GPa. Conversely, while less consistent the SNAP potential tended to over-predict the DFT computed values, however, it was closer to the DFT magnitude on more occasions relative to the MTP potential. Unfortunately, the SNAP potential exhibited undesirable deviations from the DFT values in select composition ranges. Specifically, in compositions rich in Ta (typically $\gtrsim$ 32 at.%), the calculated elastic constants exhibited a high level of imprecision, causing the calculated moduli to significantly deviate from the apparent trends forming at lower Ta concentrations. Because of this flaw, the MTP potential was used instead to model the elastic constant matrix in the optimization bulk modulus calculations. While the overall magnitude of the MTP moduli are too low, they're trend and behavior as the composition is varied is remarkable stable, and in every case precisely mimics the general trend of the DFT moduli, thus we believe the MTP potential should allow for the true optimization of the elastic moduli. Likewise, because of the relative consistency of the calculated bulk moduli (via both MTP-MD and DFT), the bulk modulus was chosen as the explicit objective for elastic optimization in this work.

Thermal Expansion

For thermal expansion (α_L), calculations, the MTP and SNAP potential were benchmarked against rule of mixtures (ROM) predictions based on experimentally measured lattice constants at 298 and 573 K[1]. In Supplementary Figure 2, the two ROM α_L predictions are plotted alongside the MTP and SNAP predictions of α_L, which were determined by incrementally increasing the temperature from 0 K to over 1200 K, and modeling the change in lattice constant through NPT ensemble calculations. Similarly, to the $\mathbb{C}_{ijkl}$ calculations, the parameterization and size of the supercell in the MD calculations was identical the optimization α_L calculations. The MTP potential outperformed the SNAP potential (by predicting closer to the ROM predictions) in three of the four compositions, while in the fourth (a Ta heavy composition), the ROM predictions lied almost exactly between the MTP and SNAP predictions. Also of note, the MTP predictions near 200-400 K were noticeably more stable, showing greater precision and consistency.

BCC Retention

Benchmarking the accuracy of the dynamic shock loading calculations was not possible as there is no relevant experimental data in literature to compare with. Instead we report on our experience using each potential to determine BCC % retention. Our decision to use the SNAP potential for shock calculations during optimization was based on two things. First, we developed the SNAP potential specifically to model highly strained systems by including a compositionally robust sampling of uniaxially and volumetrically strained systems in the DFT training data. (See McCarthy et al.[2] for details of the SNAP potential training). Secondly, in MD simulations informed by the MTP potential, we found that the shock wave failed to produce any meaningful or measurable amount of permanent deformation. The shock wave would travel through the structure, momentarily deforming atomic positions, however, the atoms would always return to a near perfectly pristine BCC state once the shock wave had passed. We found this to be the case regardless of the simulation cell size, initial temperature of the of the system, or the speed of the piston (observing the same behavior even up to 1200 m/s piston velocity).

As the size and shape of the supercell used to model shock deformation can have a significant effect on the final deformation behavior, we show BCC% convergence as a function of supercell X and Y unit cell repetitions in Supplementary Figure 3. We converged the simulation supercell size for two compositions, one high in Mo, expected to show little deformation, and one high in Ti, expected to show a large amount of deformation. We found that simulation box size was effectively converged around 22 unit cell repetitions in the X and Y directions. Additionally, the BCC% values shown here were calculated as averages of three simulations, and so the error bars indicate the standard deviation of the BCC% metric for a single composition modeled three times with unique atomic orderings. Overall, we find generally good consistency and precision in the BCC% measurement, indicating that during optimization we could model the BCC% objective using only a single shock calculation per composition.

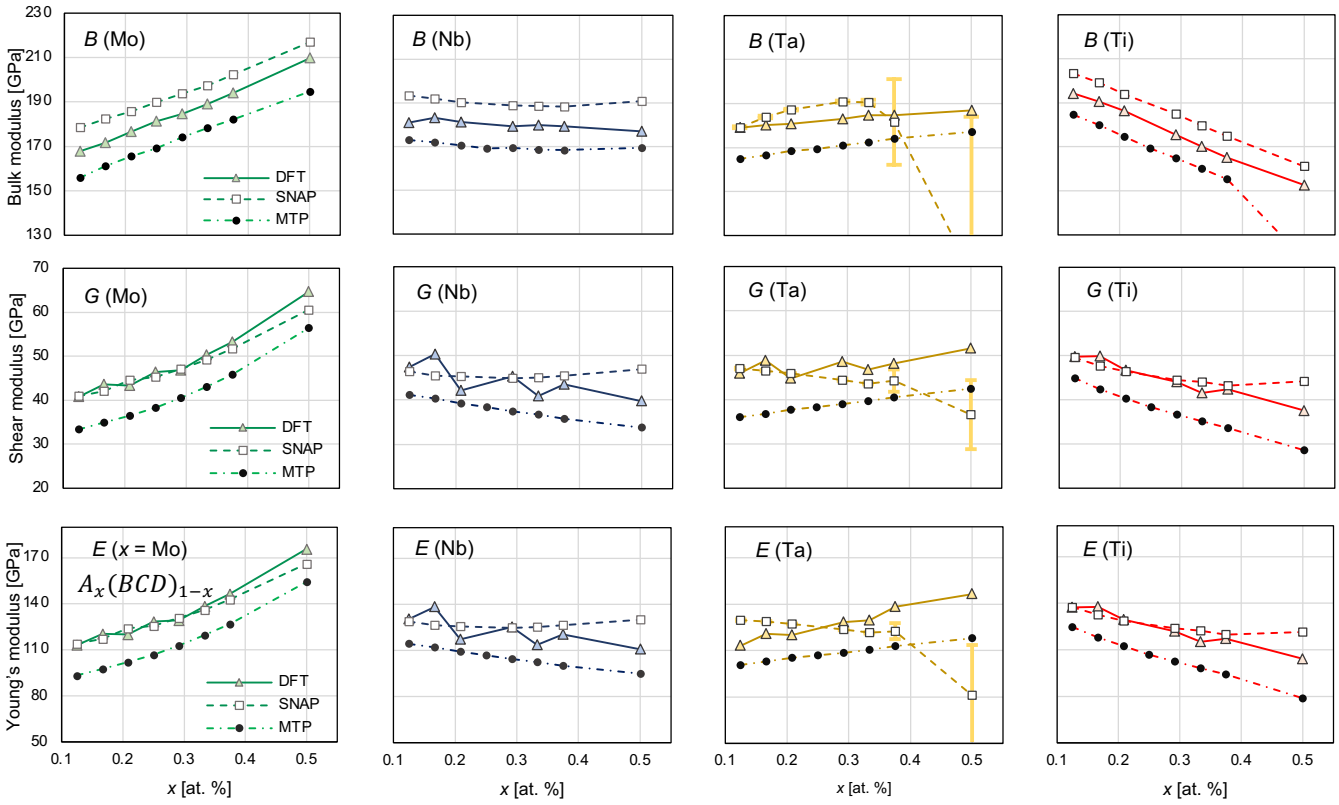

Supplementary Figure 1. Interatomic potential performance in elasticity calculations. The MTP and SNAP potential are benchmarked against DFT calculations. The $\mathbb{C}_{ijkl}$ elastic constant matrix is obtained from finite difference calculations and used to determine the Voigt-Reuss-Hill Bulk (B), shear (G), and Young's (E) moduli (displayed by row). Each panel depicts the change in B, G, and E, as the concentration of one elemental species in the alloy is incrementally changed, according to the formula $A_x(BCD)_{1-x}$, such that each column depicted the effects of one species variation.

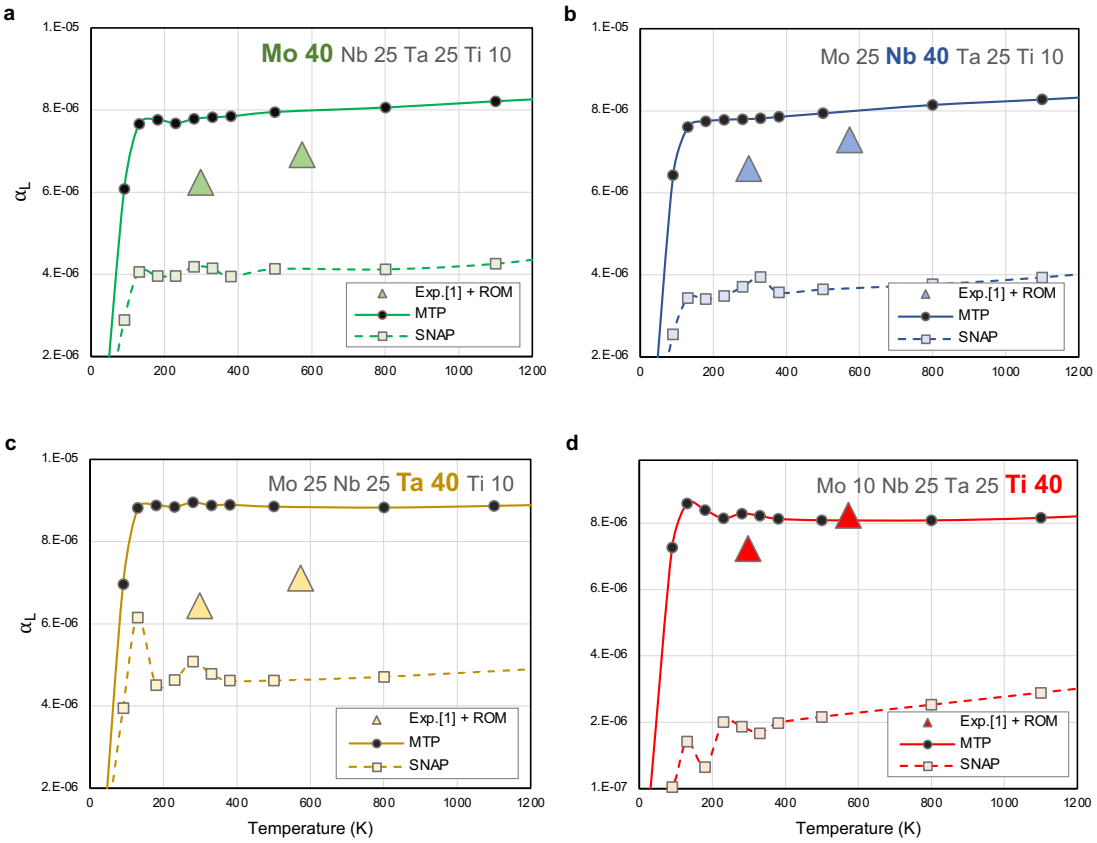

Supplementary Figure 2. Interatomic potential comparison in thermal expansion calculations. Thermal expansion (α_L), was calculated using the MTP and SNAP potentials over temperatures ranging from 0 K to over 1200 K, and benchmarked against ROM α_L predictions made using experimentally measured lattice constants at 298 and 573 K[1]. Each panel depicts the MD and ROM α_L predictions for selected alloy composition, in which the concentration of one element was increased and the concentration another element (typically Ti) was decreased.

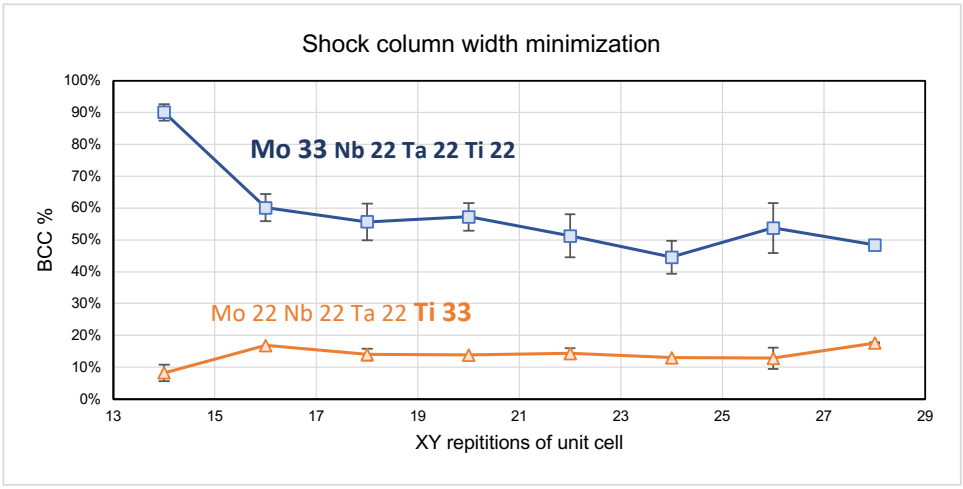

Supplementary Figure 3. Shock column width convergence. The variation in BCC% retention after shock loading was modeled as a function of the number of unit cell replications in the X and Y directions, perpendicular to the direction of the shock wave movement. Two compositions were considered, one high in Mo and the other high in Ti, finding convergence around 22 XY replications. Error bars indicate the standard deviation in BCC% for three separately modeled, uniquely ordered random structures.

Note 2: Insights on configurational entropy

Property correlations

In Supplementary Figure 4, we explore the relationships between B, α_L, C_P with configurational entropy S_{conf}. The configurational entropy S_{conf} is an important design metric in HEAs, as it is directly related to the thermodynamic stability of ground state phases. Typically, the higher the better, where traditional definitions of HEA classification require that $S_{conf} > 1.5R$ (where $R = 8.314$ J/mol·K is the ideal gas constant)[3]. In the the four element design space MoNbTaTi, only the equiatomic (denoted by the black triangles in Supplementary Figure 4) and near-equiatomic compositions come even close to this metric. Under these definitions every compositional configuration explored in this work would fall within a range more typical of medium entropy alloys ($1 - 1.5R$). However, more recently the definition of HEAs in relation to configurational disorder has come to take on some fluidity, with anything $> 1.0R$ generally able to be discussed as high-entropy[4]. Of the Pareto optimal alloy compositions discovered in this work, S_{conf} typically falls between 9 and 10.5 J/mol·K, and can be considered high-entropy under this newer criteria. Conversely, compositions that yield optimal property configurations typically lie far from the equiatomic region of the design space (Supplementary Figure 4d), and so the improvement of property performance comes at the cost of slight configurational destabilization.

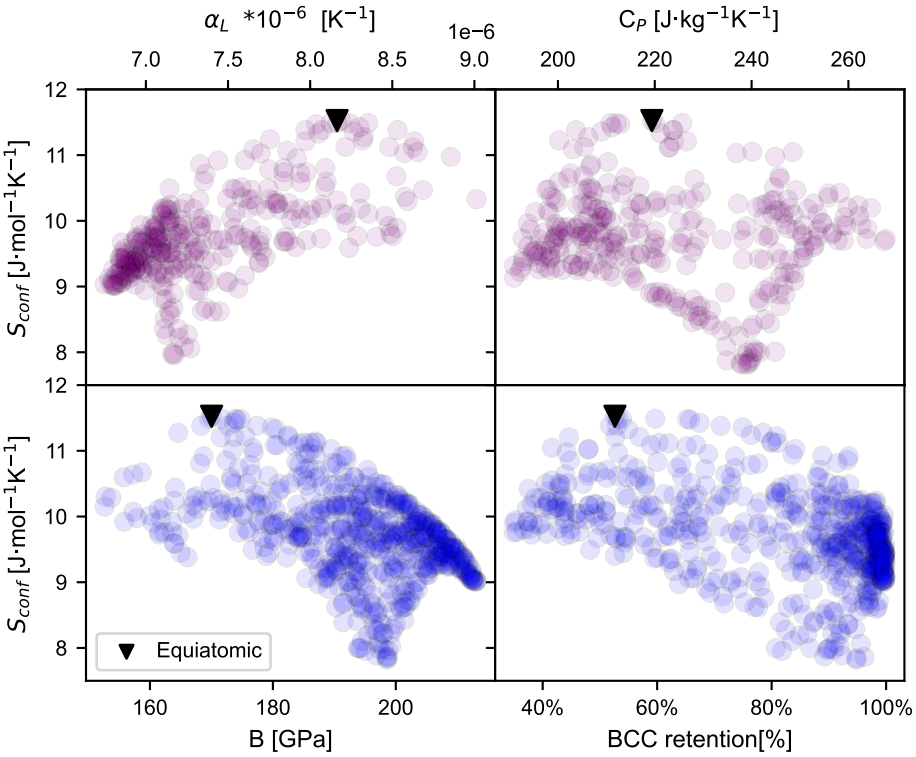

Supplementary Figure 4. Relationship between entropy and objective properties. The configurational entropy (S_{conf}) is calculated for every modeled composition and plotted against their respective bulk modulus (B), coefficient of thermal expansion (α_{L}), heat capacity (C_{P}), and BCC% retention. The properties of the equiatomic composition are denoted by upside down arrows.

Note 3: Insight on compositional effects

Where the previous compositional analyses were focused only on points within the Pareto optimal solution sets, the compositional effects derived here encompass the entire set of modeled points from both optimizations (A and B) in this work. In Supplementary Figure 5 the effect of individual alloy component concentrations derived from optimization A are shown in the top row (a-c) and from optimization B in the bottom row (d-f). Each line was obtained as a second order polynomial fit to the raw elemental compositions plotted against each property. It should be noted that the relationships are plotted somewhat unconventionally here, with the dependent material property on the normally independent X-axis as we believe it allows for better visualization of the direct influence of individual species concentrations on an individual property. For example, in panels a and d it is very clear that greater at.% of Mo is associated with improved B values, while in panel e, it is seen that a low at.% of Ta is needed to obtain high C_P values. The plot construction here also allows one to obtain the approximate alloy composition needed to obtain a specific property value by simply drawing a vertical line at the desired value and taking the species concentrations where they cross this line. The total composition of the alloy, while only approximate, is the combination of each species value, and if tested should exhibit a property behavior replicating where the vertical line was drawn along the X-axis.

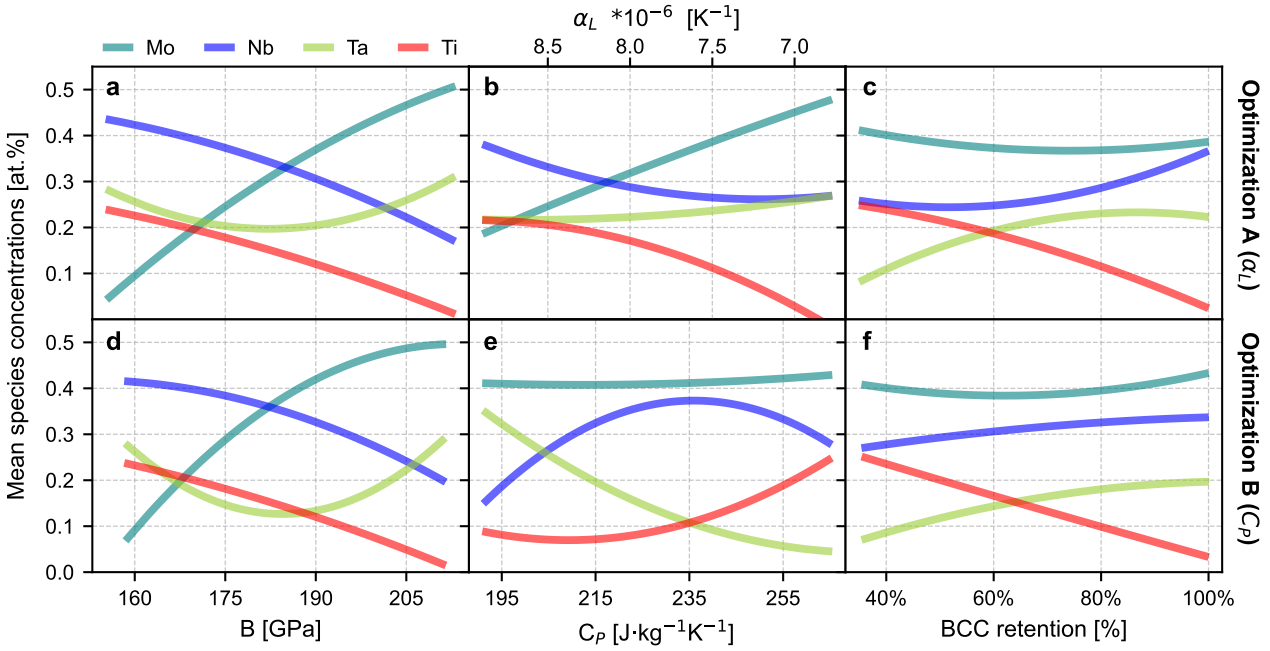

Supplementary Figure 5. Compositional breakdown of the entire performance space. Second order polynomial fits are made to between the concentration of each species and the objective properties. The panels in the top row (a-c) show concentration correlations for alloys modeled during optimization A, awhile panels in the bottom row show concentration correlations for alloys modeled in optimization B.

Note 4: Validation of molecular dynamics models through DFT

In an effort to provide some form of validation for the MD modeling used in this work, we have used DFT to calculate and benchmark the bulk modulus and heat capacity for the four alloy compositions selected from regions B-I-IV of optimization B and compared them with the respective MD based calculations. These are also compared with rule-of-mixtures (ROM) predictions based on the experimental data[5–8] (measured at the closest/most relevant temperature range we could find).

For these simulations, we used VASP along with the same parameter configuration employed for DOS calculations as already described in the Methods section. For both B and C_P calculations, a $3 \times 3 \times 4$ supercell containing 72 atoms was used along with a $3 \times 3 \times 4$ gamma-centered k-point grid. For the B modulus, the elastic constant matrix C_{ijkl} was found through the relationship between stress and strain calculated using the finite atom displacement methodology built into the VASP program. For C_P calculations, ab-initio molecular dynamics (AIMD) simulations were employed to model the alloys at high temperatures from first principles. The C_P was calculated for each alloy at 300 K following the same methodology used for the MD calculations. Each AIMD simulation employed an NPT ensemble, that allowed the volume to relax at constant temperature and pressure. Simulations were carried out for 5000 steps, at 3 fs per step, totalling 15 ps of simulation time. The final energy (used in the C_P calculation) was taken as the average of the last 2000 steps in the simulation.

Overall, we observe sizeable magnitude differences between the MD and DFT predictions, however, the relative trends predicted for both B and C_P moving from alloy B-I to alloy B-IV are remarkably consistent (as shown by the line plots above the bar plots). Notably, both the MD and DFT results are in moderately good agreement with the trends of the ROM predictions. The reason for the difference in magnitudes of the DFT and MD predictions is difficult to deduce, however, in the case of C_P it could potentially be related to limitations AIMD, namely small supercell sizes and short simulation times.

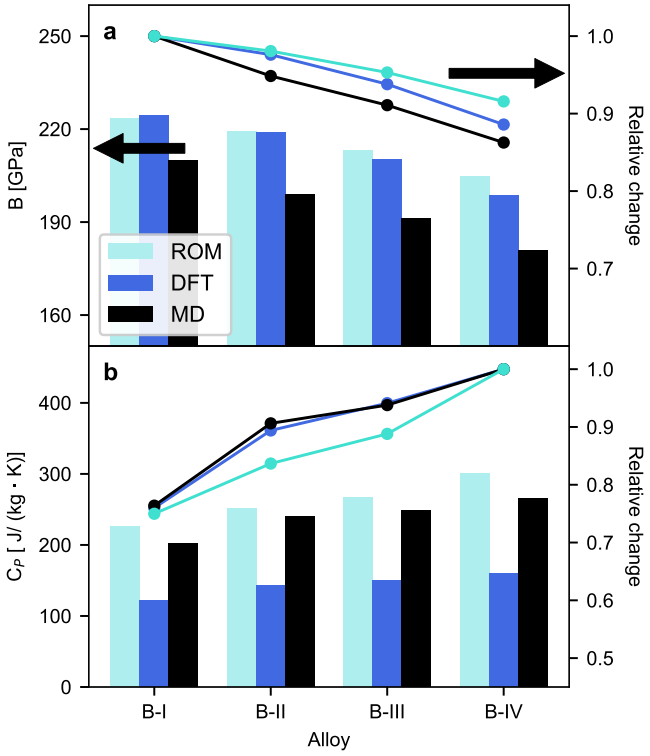

Supplementary Figure 6. MD, DFT, and rule-of-mixtures comparison. The MD methods used in this work are compared against DFT and rule-of-mixtures (ROM) predictions for the four alloys designated in regions I-IV of the optimization B Pareto front. **a** shows the bulk modulus, and **b** shows the heat capacity. The bar plots show the true value of each property and corresponds to the left axis while the lines, corresponding to the right axis, show the normalized values depicting the relative trend exhibited by each method of calculation. Despite magnitude differences, the relative trends are remarkably similar.

Acknowledgements

This work is supported in part by the Center for Integrated Nanotechnologies, an Office of Science user facility operated for the U.S. Department of Energy. This article has been authored by an employee of National Technology & Engineering Solutions of Sandia, LLC under Contract No. DE-NA0003525 with the U.S. Department of Energy (DOE). The employee owns all right, title and interest in and to the article and is solely responsible for its contents. The United States Government retains and the publisher, by accepting the article for publication, acknowledges that the United States Government retains a non-exclusive, paid-up, irrevocable, world-wide license to publish or reproduce the published form of this article or allow others to do so, for United States Government purposes. The DOE will provide public access to these results of federally sponsored research in accordance with the DOE Public Access Plan https://www.energy.gov/downloads/doe-public-access-plan.

Supplementary References

[1] Touloukian, Y. S., Kirby, R., Taylor, R. & Desai, P. Thermal expansion: metallic elements and alloys (1975). URL https://www.osti.gov/biblio/5439716.

[2] McCarthy, M. J., Startt, J., Dingreville, R., Thompson, A. P. & Wood, M. A. Atomic representations of local and global chemistry in complex alloys. Preprint at: https://doi.org/10.48550/arXiv.2303.04311 (2023).

[3] Murty, B. S., Yeh, J.-W., Ranganathan, S. & Bhattacharjee, P. P. *High-Entropy Alloys* (Elsevier, 2019). URL https://doi.org/10.1016/C2013-0-14235-3.

[4] Yan, X., Liaw, P. K. & Zhang, Y. Order and disorder in amorphous and high-entropy materials. *Metallurgical and Materials Transactions A* **52**, 2111–2122 (2021). URL https://doi.org/10.1007/s11661-021-06250-4. DOI 10.1007/s11661-021-06250-4.

[5] Featherston, F. H. & Neighbours, J. Elastic constants of tantalum, tungsten, and molybdenum. *Physical Review* **130**, 1324 (1963). URL https://doi.org/10.1103/PhysRev.130.1324. DOI 10.1103/PhysRev.130.1324.

[6] Hubbell, W. & Brotzen, F. Elastic constants of niobium-molybdenum alloys in the temperature range -190 to +100 °C. *Journal of Applied Physics* **43**, 3306–3312 (1972). URL https://doi.org/10.1063/1.1661712. DOI 10.1063/1.1661712.

[7] Allard, S. *Metals: Thermal and Mechanical Data* (Elsevier, 2013).

[8] Chase, M. W. NIST–JANAF thermochemical tables 4th ed. *Journal of Physical and Chemical Reference Data* **25**, 1069–1111 (1996).